Earth and Planetary Science Letters 275 (2008) 221–232

Contents lists available at ScienceDirect

Earth and Planetary Science Letters

journal homepage: www.elsevier.com/locate/epsl

Topographic site effects and the location of earthquake induced landslides

Patrick Meunier *, Niels Hovius, John Allan Haines

Department of Earth Sciences, University of Cambridge, Downing street, CB2 3EQ, Cambridge, UK

ARTICLE INFO

Article history:
Received 8 April 2008
Received in revised form 8 July 2008
Accepted 13 July 2008
Available online 23 July 2008

Editor: R.D. van der Hilst

Keywords:
landslides
earthquake
site effects
ground motion
natural hazards

ABSTRACT

In the epicentral areas of major recent earthquakes, landslide density scales with peak ground acceleration. Topographic site effects on seismic waves are known to cause important gradients in ground acceleration in individual mountain ridges. Using landslide maps from the epicentral areas of earthquakes near Northridge, California, Chi-Chi, Taiwan, and the Finisterre Mountains of Papua New Guinea, we have investigated the control of these site effects over the location of earthquake induced slope failure. In our examples, earthquake-triggered landslides clustered near ridge crests, where the susceptibility to landsliding was greatest. This pattern is strongest in the Northridge epicentral area, and secondary landslide clusters were found in colluvial slope toes in western Taiwan and above inner gorges in the Finisterre Mountains. In contrast, rainfall-triggered landslides in the western Southern Alps of New Zealand were evenly distributed over all slope segments, and the landslide susceptibility was lowest near ridge crests. Observed patterns of earthquake induced landsliding are consistent in a diverse geological substrate. They correlate with the distribution of very steep slopes in the epicentral areas, but we demonstrate that topographic site effects can also be a strong control. Using the impedance operator method, we have modeled the propagation of seismic waves in a generic ridge-and-valley topography with and without inner gorge. This topography has little effect on incoming P waves, but a strong effect on S waves, giving rise to a significant amplification of peak ground accelerations at or near ridge crests, and at convex knickpoints within ridge flanks. The preferential orientation of landslides away from earthquake epicenters in the Finisterre Mountains and central west Taiwan is likely caused by asymmetric amplification of oblique incoming seismic waves across mountain ridges, and indicates that topographic site effects have dominated over topographic controls on landslide location in these areas. Although orientation of landslides in the Northridge area does not conform with this interpretation, our results suggest that knowledge of topographic site effects and the attenuation of seismic waves can be an important tool in the prediction of spatial patterns of earthquake induced landsliding.
Crown Copyright © 2008 Published by Elsevier B.V. All rights reserved.

1. Introduction

Landsliding is the dominant mass wasting process in all upland areas where the rate river cutting is greater than the rate of rock weathering on hillslopes (Burbank et al., 1996; Hovius et al., 1997, 2000). Moreover, globally, landslides are the primary cause of damage and loss of life associated with severe storms and earthquakes in mountainous terrain (Swiss Re, 2000). Although progressive undercutting of valley sides due to channel incision can provide a sufficient condition for slope failure (Kelsey, 1988), most landslides are induced by earthquakes (e.g., Oldham, 1899; Keefer, 1984, 1994; Harp and Jibson, 1996) (Fig. 1), rainstorms (Iverson, 2000), or a combination of these two (Dadson et al., 2004). Seismic accelerations cause short-lived disturbances in the balance of forces within hillslopes that may induce slope failure. The radius of the area affected by landslides, and the intensity of landsliding within this area increase with the magnitude of an earthquake (Youd and Perkins, 1978; Keefer, 1984, 2000), and where sufficient data is available, the density of earthquake induced landslides is linearly and highly correlated with measured peak ground accelerations (Meunier et al., 2007). As seismic waves attenuate with distance from source, the density of earthquake induced landslides decreases systematically away from the earthquake epicenter over a distance of tens of kilometres (Keefer, 2000, 2002; Dadson et al., 2004; Meunier et al., 2007). On shorter length scales, topographic relief has a profound influence on the propagation of seismic waves, giving rise to distinct zones of amplification or damping of ground acceleration in specific topographic locations (Benites and Haines, 1994; Bouchon et al., 1996). If the relation between landslide density and peak ground acceleration, observed on a regional scale, also holds at the scale of individual mountains and ridges, then the pattern of earthquake induced slope failure is expected to reflect the topographic site effects on seismic waves.

In this paper, we consider patterns of earthquake induced landslides in the context of seismic wave field models and observations of the amplification of strong ground motion in ridge-and-valley topography, and compare these patterns with those of rain induced

* Corresponding author.
E-mail address: pmeu05@esc.cam.ac.uk (P. Meunier).

0012-821X/$ – see front matter. Crown Copyright © 2008 Published by Elsevier B.V. All rights reserved.
doi:10.1016/j.epsl.2008.07.020

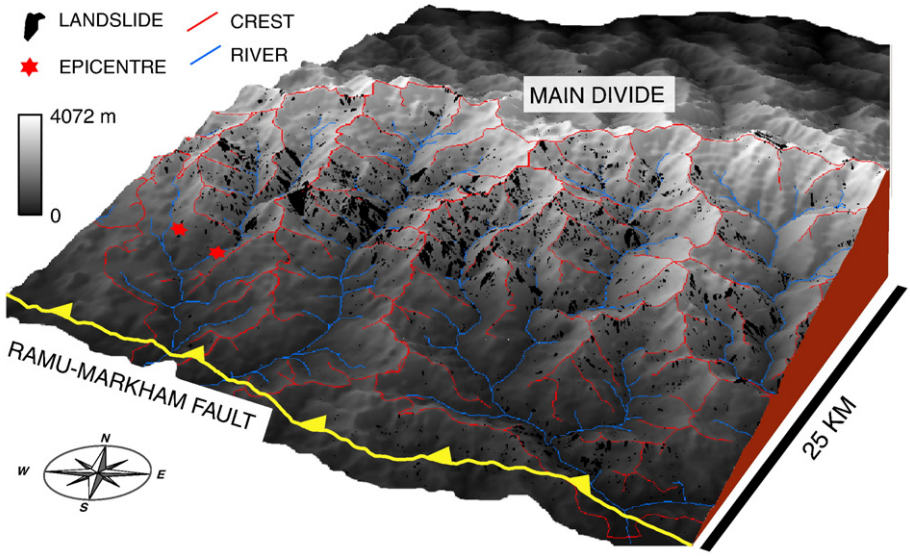

Fig. 1. Digital relief model of the western Finisterre Mountains, Papua New Guinea, showing the location of >5000 mapped landslides triggered by two earthquakes with magnitudes of M_w 6.7 and 6.9 in 1993 on the Ramu-Markham Thrust.

landslides in the same and other areas to identify unique attributes of earthquake induced landslide populations. Using data from Taiwan, Papua New Guinea, California, and New Zealand, we show that earthquake induced landslides cluster on major convexities in the topography, and that slopes facing away from an earthquake source are especially prone to failure. These findings have important implications for the topographic evolution of landscapes exposed to significant seismicity, and for the mitigation of risks associated with earthquake and landslide hazards.

2. Slope failure and topographic site effects

Hillslope failure occurs when the shear stress across a potential failure plane exceeds the substrate strength. Fundamentally, the stability of a hillslope is determined by its surface gradient, the density, cohesion and frictional properties of its substrate, the depth of potential failure plains, and the gravitational acceleration (Carson and Kirkby, 1972). A change in any of these parameters can cause the destabilization and failure of a slope. For example, the topographic gradient may increase due to undercutting by river erosion at the base of a slope. Similarly, the substrate frictional or cohesive strengths may decrease by weathering, or wetting of the rock mass, which also increases the density of the slide block. Earthquakes affect the stability of slopes in two ways. First, seismic shaking may cause loss of cohesion and/or reduction of the frictional strength of the substrate by shattering of rock mass or liquefaction in soft, saturated soils. Widespread shattering has been reported from the epicentral areas of many large earthquakes associated with thrusting, and appears to be especially severe in topographic slopes located on the hanging wall (Brune, 2001). Coalescence of cracks during earthquakes gives rise to increased substrate permeability and has caused the release of vast volumes of groundwater from epicentral areas (Wang et al., 2004). Liquefaction of soft sediments has been observed, for example, in the San Francisco Bay area during the 1989 Loma Prieta earthquake (Kayen et al., 1998). Second, addition of seismic accelerations to the ambient, gravitational acceleration results in short-lived and episodic changes of the normal and shear stresses in hillslopes during earthquakes. These changes may be sufficient to cause failure.

Unexpectedly large peak vertical accelerations have been recorded at ridge crests during several earthquakes, not necessarily very large ones. For example, during the 1987 Whittier Narrows, California, earthquake, the amplitude of seismic waves recorded at the crest of Tarzana Hill, a 60 m high feature located 44 km from the epicenter, was ten times greater than that observed on the surrounding plains (Spudich et al., 1996). On the same hill, instruments recorded a peak horizontal acceleration of 1.78 g, during the 1994 Northridge earthquake (Shakal et al., 1994; Bouchon and Baker, 1996). This is one of the largest accelerations ever measured in an earthquake. Topographic amplification of ground accelerations occurs when seismic waves entering the base of a topographic ridge are partially reflected back into the rock mass and diffracted along the free surface. Thus, seismic waves are progressively focused upwards and the constructive interference of their reflections and the associated diffractions increases towards the ridge crest, giving rise to enhanced ground accelerations on topographic highs (e.g., Davis and West, 1973; Bouchon, 1973; Geli et al., 1988; Benites and Haines, 1994). Is this topographic site effect large enough to significantly affect the propensity to slope failure during an earthquake? To answer this question we have analyzed the location of landslides in four mountain areas bounded by seismically active faults. They are the Taiwan Central Range, the Santa Susanna and San Gabriel Mountains in California, the Finisterre Mountains of Papua New Guinea, and the western Southern Alps, New Zealand. The settings of our examples are summarized in the next section.

3. Case settings

3.1. Central west Taiwan

Taiwan's Central Range is the product of oblique collision between the Luzon Arc, on the Philippine Sea Plate, and the Eurasian continental margin. Rapid crustal shortening is accompanied by frequent large earthquakes (Pezzopane and Wesnousky, 1989), and Taiwan has a vigorous sub-tropical climate with a mean annual precipitation of 2.5 m and an average of four typhoons per year (Wu and Kuo, 1999). This gives rise to erosion rates averaging 3–7 mm yr^{-1} and locally up to 60 mm yr^{-1} (Dadson et al., 2003). The M_w 7.6 Chi-Chi earthquake, on 21 September 1999, was the largest in Taiwan for 50 yr, and the largest on the Chelungpu thrust fault in 300–620 yr (Shin and Teng, 2001; Chen et al., 2001). The earthquake had a focal depth of 8–10 km, resulted in the rupture of an approximately 100 km segment of the N–S trending, east-dipping (~30°) Chelungpu thrust, and produced recorded ground accelerations of up to 1 g (Lee et al., 2001). It caused more than 20,000 landslides with a total surface area of about 150 km^2, located in Neogene sediments and older, metasedimentary rocks (Lin et al., 2000). The

landslides were mapped by the Taiwan National Science and Technology Centre for Disaster Prevention from SPOT satellite images with a resolution of 20 m. The Chi-Chi epicentral area was hit in July 2001 by a large typhoon, Toraji, which produced a total water discharge from the Choshui River of 0.8 km^3 over two days. In 1996, 80 yr after the previous M_w>6 earthquake in the area, typhoon Herb, produced a total water discharge of 1.2 km^3 over three days from the Choshui River. Interposed by the Chi-Chi earthquake, this sequence of events represents a natural experiment that provides quantitative information about the impact of a large earthquake on the pattern and intensity of hillslope mass wasting (Dadson et al., 2004; Lin et al., in press).

3.2. Southern California, U.S.A.

Topographic relief and seismicity in southern California are associated with dextral transpression at the Pacific-North America plate boundary (Montgomery, 1993). One of the largest recent earthquakes on this system, the M_w=6.7 Northridge earthquake of 17 January 1994 occurred on a blind thrust fault, dipping southward at about 35° below the San Fernando Valley in the Los Angeles metropolitan area. It had a thrust focal mechanism with a hypocenter at 19 km depth (Hauksson et al., 1995), and triggered more than 11,000, mainly shallow landslides with a total area of 23.8 km^2, in the dry, sedimentary substrate of the Santa Susanna and San Gabriel Mountains (Harp and Jibson, 1995, 1996) where mean annual precipitation is 0.4–0.7 m. The landslides were mapped from a 30 m resolution airphotos by the U.S. Geological Survey (1995, USGS open file report; 1996, BSSA).

3.3. Finisterre Mountains, Papua New Guinea

Oblique convergence of the Australian and Pacific plates drives uplift and deformation of the Finisterre Mountains. The mountain range consists of volcanic and volcaniclastic rocks thrust over coarse foreland deposits and capped by limestones (Davies et al., 1987; Abbott et al., 1994). Bounded to the south by the Ramu-Markham thrust fault, the mountain range has attained an elevation of 4 km since onset of deformation around 3.7 Ma (Abbott et al., 1997). Its orographic effect and near-equatorial location force intense, seasonal rainfall, with mean annual precipitation rates of about 4 m at intermediate elevations. Bedrock landsliding appears to be the dominant mode of hillslope mass wasting in the range (Hovius et al., 1998; Densmore and Hovius, 2000), driven by frequent, heavy rainfall and periodic, large earthquakes on the Ramu-Markham fault. Perhaps the earliest historical record of a destructive earthquake in the Finisterre Mountains is a diary entry by Miklaucho-Maclay, dated July 1876 (in Johns, 1986): "The changes in appearance of the summits of the Mana Boro Boro (Finisterre Mountains) surprised me on my return to the coast. At my departure (in December 1872) the vegetation covered even the peaks of the range, but now in many places the summits and steep slopes were completely bare. The natives told me that during my absence there had been several earthquakes on the coast and in the mountains …". Equally destructive seismic episodes occurred on the central section of the Ramu-Markham fault in 1922 (Ripper and Letz, 1991) and October 1993 (Tutton and Browne, 1994). The latter comprised two thrust earthquakes with magnitudes of M_w 6.7 and 6.9 (Stevens et al., 1998) (Fig. 1). The earthquake focae were located at 19 and 20 km depth, less than 5 km apart. We have mapped about 4700 landslides with a total surface area of 55 km^2, triggered by these two earthquakes, from 30 m resolution SPOT images.

Although different in magnitude, the focal mechanisms and hypocenter depths of the earthquakes in California, Papua New Guinea, and Taiwan are similar: all three are shallow thrust events. This justifies a direct comparison of the patterns of landsliding associated with these earthquakes (cf. Meunier et al., 2007). To contrast these patterns, we have selected a fourth mountain range where no large earthquakes have occurred in the recent past.

3.4. Southern Alps, New Zealand

The Southern Alps mark the transpressional boundary between the Australian and the Pacific plate (Walcott, 1984). There, rock uplift rates approaching 7 mm yr^{-1} (Bull and Cooper, 1986) have assisted the building of 2 to 4 km of relief. In the steep west flank of this orographic barrier, precipitation rates reach up to 15 m yr^{-1} (Griffiths and McSaveney, 1983), driving rapid exhumation of schists and gneisses (Tippett and Kamp, 1993; Batt, 1997) on the range bounding Alpine Fault. The last M_w>7 earthquake on the central segment of the Alpine Fault occurred around 1826 AD (Wells et al., 1999). Since then, this fault segment has only had minor seismicity, and recent landslides have been induced mainly by rainfall. Hovius et al. (1997) have mapped about 5000 landslides with a total area of 74 km^2 in a 2670 km^2 segment of the western Southern Alps from 1:50,000 air photos covering a time interval from 1948 to 1986, and they demonstrated that bedrock landsliding is the principal mode of hillslope mass wasting (cf. Korup, 2006).

4. Position of landslides and propensity to slope failure

First, we consider the topographic location of landslides in these four areas. The available landslide data does not permit distinction between landslide scars and deposits. Therefore, the position of a landslide is described by three parameters: 1) the distance from the highest point on the landslide crown to the top of the slope on which it is located; 2) the distance separating the toe of the landslide deposit from the nearest river channel; and 3) the length of the landslide measured along the line of steepest descent. To measure the first two quantities, the ridge and stream networks in a landscape must be known. Using a characteristic break in the scaling relation of local slope and upslope area (cf. Montgomery, 2001), the transition from the hillslope domain, where gravitational processes dominate, to the fluvial domain can be determined from a digital elevation model (DEM) (Fig. 2). In landslide-dominated hillslopes, the local topographic gradient is only weakly dependent on the upslope area producing runoff through a point. In rivers, the local channel gradient decreases systematically downstream to produce a distinct, concave-up longitudinal profile. In the Finisterre Mountains the transition from hillslope to channel typically occurs where the upslope area is about 3.2 ± 1 km^2. The hillslope-channel transition is at 1.1 ± 0.3, 0.89 ± 0.2, and 1.5 ± 0.5 km^2 in central west Taiwan, the Santa Susanna Mountains, and the western Southern Alps, respectively. In our analysis we have assumed that all points with upslope area smaller than this cutoff are located on hillslopes, and all points with greater upslope areas in channels. In reality, slope lengths are not uniform, and the

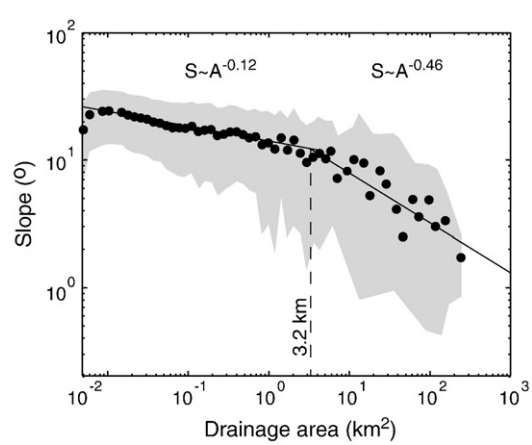

Fig. 2. Plot of local slope, S, against upslope area, A, for the western Finisterre Mountains. Filled circles show the mean slope measured in the direction of steepest descent within logarithmically spaced bins of upslope area, and the standard deviation of local slope values is indicated in grey. The break in scaling is interpreted as the transition from hillslopes (A<3.2 km^2) to fluvial channels (A>3.2 km^2).

assumption has limited the precision of our analysis. The position of topographic ridges has been pinned by the change of sign of the second derivative of the DEM topography, with manual adjustments in rare equivocal cases. The second derivative of the topography is calculated over three adjacent DEM cells, setting the accuracy of automated ridge mapping to about 100 m. Fig. 1 shows the ridge and channel networks in the Finisterre Mountains as determined by these procedures.

Within the context of these networks, flow distances from all cells in the landscape, including those in landslides, from the nearest ridge (d_{top}) and to the nearest stream (d_{st}) have been extracted from DEMs using a flow path routine. Measured distances were normalized by the total length of the slope using

$$|d_{\mathrm{st,top}}| = \frac{d_{\mathrm{st,top}}}{d_{\mathrm{st}} + d_{\mathrm{top}}}. \quad (1)$$

$|d_{\mathrm{st}}|$ varies from 0 for a cell located in the stream network to 1 for a ridge cell. $|d_{\mathrm{top}}|$ varies in the opposite way. The normalised data can be used in two ways. One is to look at the relative position of landslides in the landscape, and the other is to evaluate the landslide susceptibility of slope segments.

4.1. Landslide position

In Fig. 3 we have reported the position of the highest and lowest point of individual landslides in a frame of abscissa $|d_{\mathrm{top}}|$ and ordinate $|d_{\mathrm{st}}|$, indicating the size of a landslide by means of a circle with variable diameter. Landslides located along the *y*-axis have originated near or at a ridge crest, and landslides along the *x*-axis have connected with a river channel. Landslides near the origin of the plot have cleared a slope from ridge crest to river, and landslides far from both axes are in a mid-slope position.

Landslides induced by the Northridge earthquake (Fig. 3a) are strongly clustered near ridge crests. In fact, 56% of the landslides originated in the upper quart of slopes, compared to 11% in the lower quart. Only 2% of the landslides with crowns in the top quart of a slope

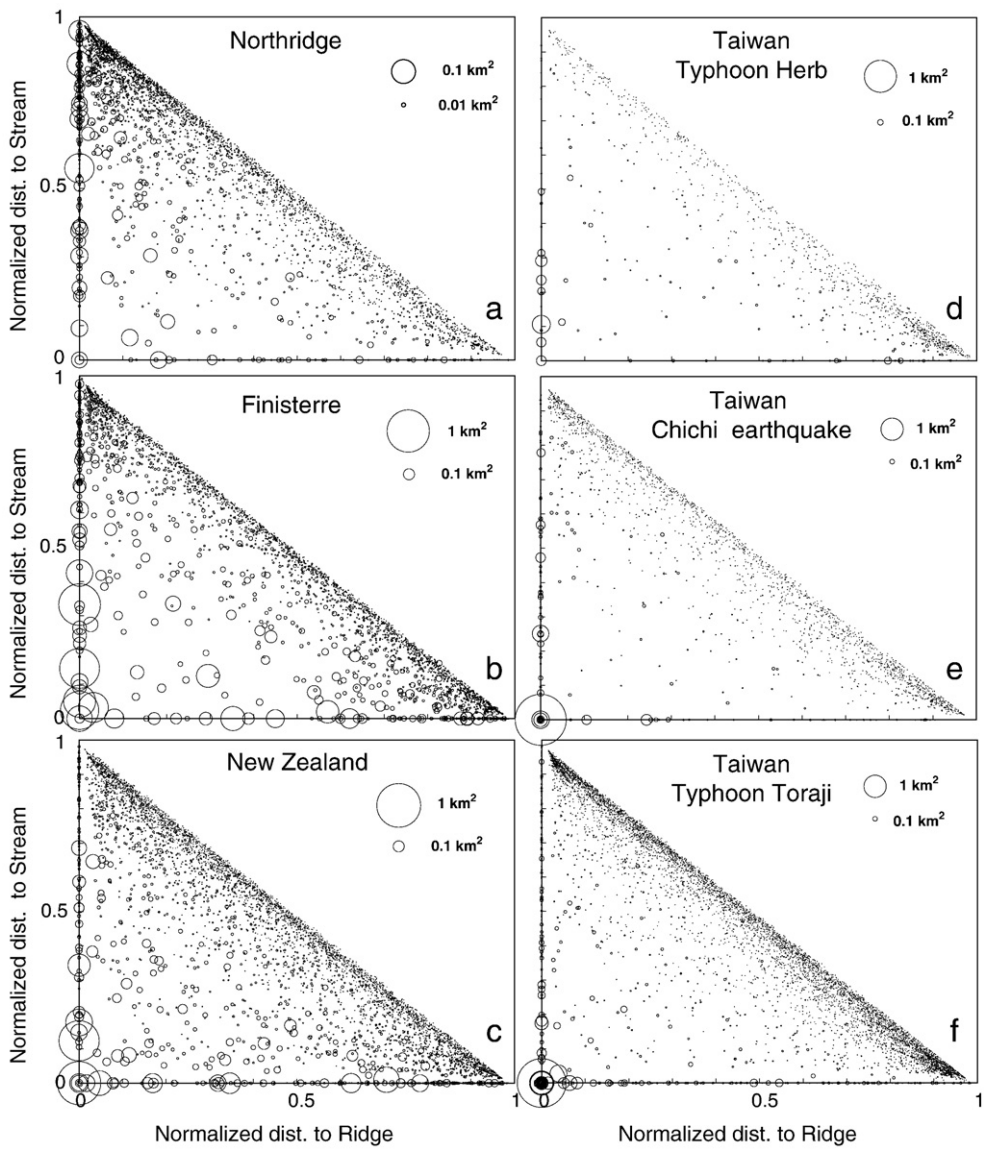

Fig. 3. Location of landslides with respect to ridge crest and stream. Distances from the landslide crown to the nearest ridge and from the lowest point on the landslide lobe to the nearest stream have been measured along the line of steepest descent, and normalized for the total length of the slope on which the landslide is located. The size (surface area) of the landslide is indicated with a circle of variable diameter. Landslides triggered by the Northridge earthquake (a) cluster around ridge crests. Landslides triggered by the 1993 earthquakes in the Finisterre Mountains (b) cluster at ridge crests and near the base of slopes. Rainfall-induced landslides in the western Southern Alps, New Zealand (c) are uniformly distributed. In central west Taiwan, landslides caused by typhoon Herb in 1996 (d) are clustered near streams, while the 1999 Chi-Chi Earthquake (e) triggered a significant number of landslides near ridge crests. The fingerprint of this shift toward the top of the slopes is still visible in the distribution of landslides triggered by typhoon Toraji in 2001) (f).

reached the lower quart of the slope. Hence most debris of earthquake induced landslides has remained on hillslopes in the epicentral area after the Northridge earthquake.

In the Finisterre Mountains, landslides triggered by the 1993 earthquakes exhibit a double clustering (Fig. 3b). 33% of landslides originated in the upper quart of slopes, and 29% in the lower quart. 3% of landslides were slope clearing. Rainfall-induced landslides in New Zealand (Fig. 3c) were uniformly distributed by comparison, with 25 ± 2% originating in each of the four slope quarts.

In Taiwan, landslides triggered by typhoon Herb in 1996 (Fig. 3d) clustered at the base of slopes. 47% of all failures started in the lower quart and only 18% in the upper quart, of which 7% reached the lower quart. During this typhoon hillslopes and channels were effectively connected and a significant portion of all landslide debris was delivered direct to rivers. In sharp contrast, landslides triggered by the Chi-Chi earthquake (Fig. 3e) in the same area had essentially the same double clustered distribution as found in the Finisterre Mountains with 34% of landslides originating in the upper quart of slopes and 28% in the lower quart. In the population of landslides triggered by typhoon Toraji in 2001 (Fig. 3f), clustering in the upper slope quart was weaker but still present at 28%, whereas the share of landslides in the lower quart had dropped to 24%. However, importantly, the number and density of landslides triggered by typhoon Toraji was much greater by comparison to typhoon Herb, even though the latter had the higher peak rain intensity and total precipitation. It is in this increased post-seismic landslide rate and the shift of landslide locations to higher slope positions that the effect of the earthquake is borne out (cf. Lin et al., in press).

4.2. Landslide susceptibility

Although the graphs in Fig. 3 show the position of individual landslides in the landscape and their clustering, they cannot be used to evaluate the susceptibility of particular slope segments to landsliding for two reasons. One, the total area of slope segments within a given distance range from stream is not uniform in distance from stream, and two, landslides do not have a uniform width, and their exact shape determines where they act on the topography. These aspects are not included in the position analysis above. To gain insight into the spatial pattern of the susceptibility of slopes to landsliding we have defined a probability ratio

$$R_P = \frac{P(|d_{st}|)_{ls}}{P(|d_{st}|)_{topo}}, \quad (2)$$

where $P(|d_{st}|)_{ls}$ is the probability of a topographic cell affected by landsliding being at a given normalized distance to stream $|d_{st}|$ and $P(|d_{st}|)_{topo}$ is the probability of any topographic cell being at that distance to stream. R_P thus expresses for a given landslide population the likelihood of landsliding proportional to the availability of topography. A value of $R_P = 1$ indicates that for a given trigger, landslides have sampled topography at a given distance to the stream network in exact proportion to the available topography. $R_P > 1$ indicates oversampling by landslides, etcetera.

For all four examples, the probability ratio R_P is plotted against the normalized distance to stream in Fig. 4. Landslides caused by the Northridge earthquake (Fig. 4a) primarily affected upper slopes, where their probability ratio was three times higher than near streams. ($R_P = 1.5$ at $|d_{st}| = 0.8$ and $R_P = 0.5$ at $|d_{st}| = 0$). In the Finisterre Mountains too, earthquake induced landslides oversampled the highest slopes ($R_P = 1.3$ at the ridges) but a second zone with higher than average probability ratios was found in the lowest slope segments ($|d_{st}| < 0.1$). Storm induced landslides in the Southern Alps equally affected all low and intermediate slope segments but undersampled the highest slopes ($R_P < 0.5$ for $|d_{st}| > 0.9$).

In Taiwan (Fig. 4b), the spatial pattern of the probability ratio depends on the landslide trigger type. Typhoon induced landslides

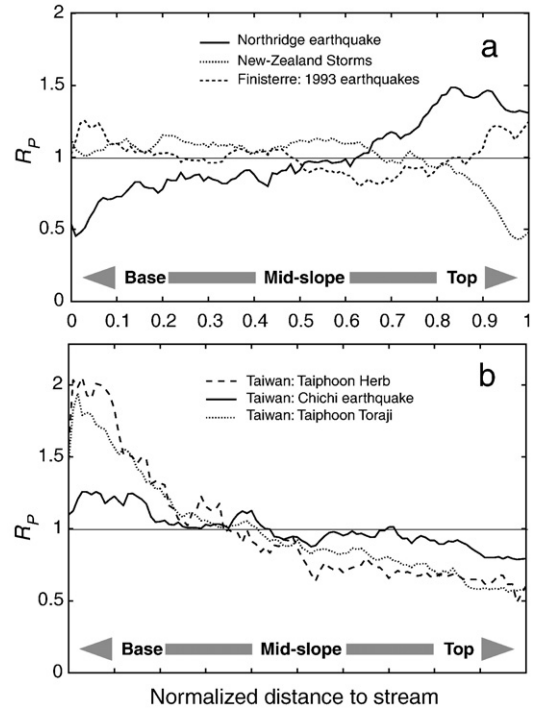

Fig. 4. Plots of landslide probability against normalized distance from stream for central west Taiwan (b) and three other study areas (a). The probability ratio R_P is the ratio of the probability of being in a landslide at a given normalized distance from stream and the probability of being somewhere in the topography at that distance from stream. The thin solid line indicates equal probability. In the Northridge epicentral area and the southern Finisterres, the highest slope segments have been affected disproportionately by earthquake induced landslides, and in central west Taiwan, high slope segments were more prone to landsliding during the Chi-Chi earthquake than during typhoons. Low slope segments were very susceptible to earthquake-triggered landsliding in Taiwan and the Finisterre mountains. In the southern Alps of New Zealand, storm triggered landslides have sampled all slope segments at a similar rate, but ridge crests were less susceptible to landsliding.

have strongly oversampled the lower quart of slopes and river banks, with R_P values of up to 2 at streams, dropping progressively to $R_P = 0.5$ at the ridges. Landslides triggered by the Chi-Chi earthquake, though following the same trend, are distributed more homogeneously along the slopes, in a marked repartitioning of landslide activity to upper slopes with respect to typhoon induced populations.

There is broad agreement between patterns of landslide position and susceptibility within regions, and a marked dependence of the landslide patterns on the trigger mechanism. In the western Southern Alps of New Zealand, where recent landslides have been triggered by rainfall, landslides were evenly distributed over all slope segments, although the susceptibility of upper slope segments to landsliding was suppressed. Elsewhere, in west Taiwan, rainfall has primarily destabilized the lowest hillslope segments that were inherently prone to landsliding. In all cases of earthquake-triggering, landslides clustered near ridge crests, where the susceptibility to landsliding was elevated or greatest. This pattern is strongest in the Northridge epicentral area, perhaps because of the dry climate and substrate. In west Taiwan and the southern Finisterre Mountains secondary landslide clusters were found in the lowest slope segments, where susceptibility to landsliding peaked.

It should be noted, again, that our data does not permit the distinction of locations of slope failure and deposition of landslide debris, although they impact the landscape in fundamentally different ways. Runout of landslides has skewed our results towards low locations within the topography, and the elimination of landslide deposits from our analysis, when permitted by the data, would result in a marked strengthening of the signature of landslide clustering and reveal a high susceptibility to failure of the highest hillslope segments

during earthquakes. However, the clustering of earthquake-triggered landslides on low slope segments in the Taiwan and Finisterre Mountains is not entirely due to landslide runout. In both cases, a disproportionate number of landslides have started low on hillslopes, indicating a high susceptibility to *failure* as well as landslide impact. Thus, the pattern we should seek to explain is one of clustering of earthquake-triggered landslides near topographic ridges and in some cases on specific, lower slope segments.

5. Causes of landslide clustering

The stability of hillslopes is controlled by their topographic gradient, the mechanical properties of the substrate, pore fluid pressures, and gravitational and transient accelerations. On short time scales, the topography of a hillslope and its interior geology may be assumed constant, but other conditions change due to rainfall and seismicity. Clustering of seismically-induced landslides may therefore be due to an intrinsic property of the landscape within which they occur, and/or the systematic spatial pattern of a transient perturbation of this landscape.

Our landslide data sets have been collected in large areas with variable geology. Although it is clear that geology is a strong control on local landslide patterns (e.g., Lin et al., in press), it is not a cause of the regionally persistent clustering of landslides described above. Similarly, rainfall can be excluded as an immediate cause of the observed clustering of earthquake-triggered landslides, because it did not rain heavily during the earthquakes in question. However, longer-lived patterns of groundwater flow may well give rise to spatial gradients in the susceptibility to slope failure. In periodic ridge-and-valley topography, gravity driven groundwater flow is directed vertically downward through ridges. Where its passage is impeded by impermeable or fully saturated rocks at depth, groundwater is forced to flow laterally. Flow from adjacent ridges may converge beneath intervening valleys, leading to outward-directed flow near valley floors. The consequent elevation of groundwater levels and pore fluid pressures, and the associated seepage forces (cf. Iverson and Reid, 1992) could give rise to enhanced failure potential towards the base of valley sides. This effect is difficult to demonstrate and it is certainly not the cause of clustering of earthquake-triggered landslides near ridge crests. Therefore, we focus our attempt to explain the observed landslide patterns on the characteristics of the topographies within which they have been found, and the expected patterns of seismic strong ground motion within these topographies.

5.1. Topography

Of all attributes of topography, local slope is likely to be the strongest control on landsliding. We have measured local slope as the steepest topographic gradient in a space of three by three DEM cells, and determined the normalized distance to stream $|d_{st}|$ for each point in our study areas. This allows calculation of the mean topographic gradient at a given normalized distance to stream. Slope lengths vary considerably within each study area. They are quasi-normally distributed with near identical mean and modal slope lengths (Fig. 5d). To eliminate the dispersion caused by very long and very short slopes

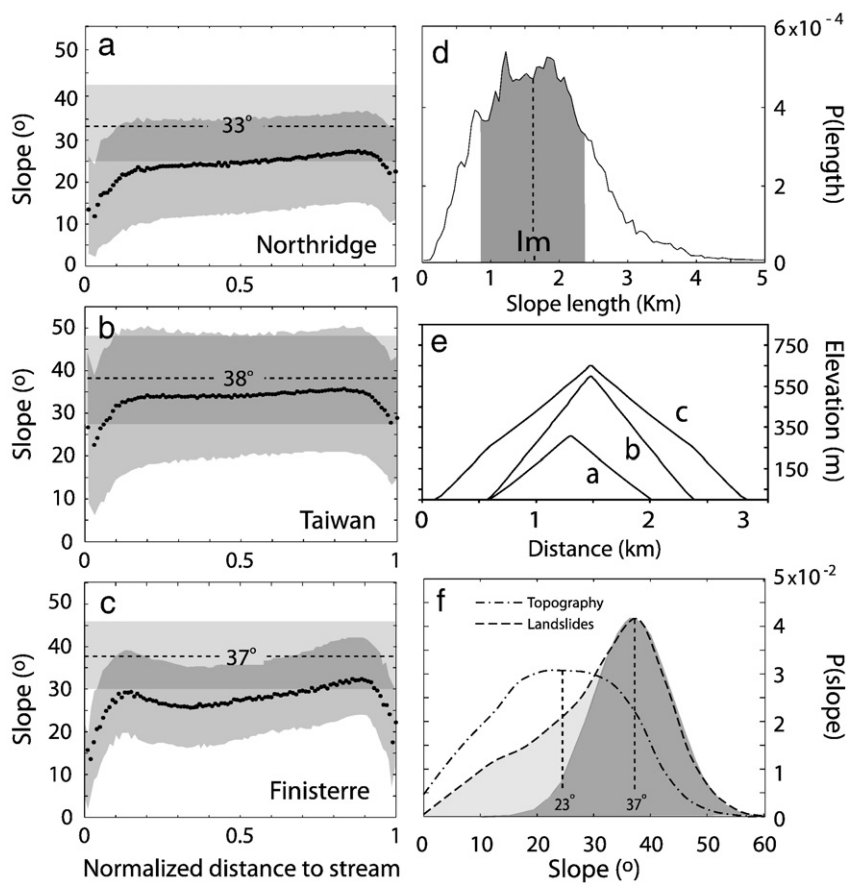

Fig. 5. a–c: Evolution of the average local topographic gradient of slopes with normalized distance to stream in the Northridge epicentral area, central west Taiwan, and the southern Finisterre Mountains. Standard deviation is reported in grey. d: Probability distribution of slope lengths in the Finisterre Mountains: the grey shading area corresponds to the mean slope length $l_m \pm \sigma$ (68% of the data). e: Average ridge profiles built from slope–distance relations shown in (a–c). f: Probability distribution of topographic slopes and landslide slopes in the Finisterre Mountains, with Gaussian components shown in dark grey. In the Finisterres, the modal slope of the topography is 23° and the modal slope of locations affected by landslides is 37°. Relatively high incidence of landslides on shallow slopes (light grey area) may be due to landslide runout. The modal landslide slope is shown in the slope–distance plots (a–c) together with the standard deviation on the Gaussian component of the slope probability distribution.

from our analysis we have only used data from slopes of intermediate length, within one standard deviation σ from the mean slope length l_m (68% of all slopes). It is assumed that these intermediate length slopes represent the common characteristics of the mountainsides of an area. In the Northridge epicentral area l_m = 0.73 km, in central west Taiwan l_m = 1.1 km, and in the southern Finisterre Mountains l_m = 1.6 km. Fig. 5a–c shows the mean local topographic slope as a function of normalized distance to stream for the three earthquake epicentral areas, and in Fig. 5e these mean slope distributions have been translated into a cross section of the average topographic ridge in each of the areas, scaled to the mean slope length l_m of the area.

In each case, the average topographic ridge has a triangular cross section, with slightly concave-up sides, as slopes steepen towards the ridge crest. The ridge crests are rounded on a scale larger than the length scale of the slope estimates, implying that this is not an artifact. Rounding is also found at the base of the ridge, possibly due to the presence of colluvial and alluvial deposits. The slope profiles of the Northridge and Taiwan ridges are smooth, but the Finisterre ridge is articulated with a steepened, convex-up section above the concave-up slope toe. This reflects the pervasive presence of inner gorges and prominent, high strath terraces along the trunk streams of the southern Finisterre Mountains (Hovius et al., 1998; Densmore and Hovius, 2000). Slopes are shortest, and have the lowest average gradient in the Northridge epicentral area. Above the mid-slope knickpoint, the average gradient of slopes in the Finisterre Mountains is only marginally higher than in the Northridge area, possibly reflecting similar mechanical properties of the rock mass (cf. Ramsey et al., 2006), but the average topographic ridge in the Finisterre Mountains is twice higher and wider, maybe because of the higher tectonic rates in the area. The average topographic ridge in central west Taiwan is steepest with the straightest sides.

Landslides are located on the steepest slopes in all epicentral areas. Landslide slope–frequency distributions are tight and symmetric around modal values that are higher than the average local topographic slope of the area (Fig. 5f) (cf. Lin et al., in press), although landslide runout causes a relatively high frequency of low slope values. In the Northridge epicentral area the modal landslide slope is 33°, in central west Taiwan it is 38°, and in the southern Finisterre Mountains 37°. We hypothesize that slope segments with gradients greater than the modal landslide slope are supercritical and prone to failure. The relatively low modal landslide slope in the Northridge area may be due to the progressive accumulation of weathered rock and colluvium on hillslopes under a dry climate (cf. Lavé and Burbank, 2004). This material is weak and prone to shallow failure on gentle slopes and earthquakes may play an important role in its erosion (Meunier et al., 2007). In contrast, many landslides in the other two epicentral areas were rooted in the rocky substrate.

The difference between the modal slope of locations affected by landslides and the average topographic slope is smallest in Taiwan, where a considerable portion of all slope segments appears to be supercritical. This may be a cause of the relatively flat distribution of the susceptibility to landsliding over the hillslope length during the Chi-Chi earthquake (Fig. 4). In contrast, the relative frequency of locations steeper than the modal slope of landslides increases systematically towards ridge crests in the Northridge epicentral area, matching the observed along-slope trend in susceptibility to landsliding in this area. In the Finisterre Mountains most supercritical sites are within the upper quart of hillslopes, but a secondary peak is located at 0.1–0.2 normalized distance to stream where the susceptibility to earthquake-triggered landsliding was found to be high. Thus, the distribution of very steep sites within the topographies of the epicentral areas appears to have contributed to the location of earthquake-triggered landslides. However, the degree of landslide clustering in the Northridge epicentral area is much greater than expected from our consideration of slope distributions, and the qualitative match of landslide patterns and slope patterns elsewhere also leaves room for additional controls on the location of earthquake-triggered landslides. Therefore, we turn our attention to topographic site effects on seismic wave fields.

5.2. Topographic site effects

Seismic waves traveling through mountain topography are subject to localized (de)amplification due to diffraction and interference, affecting the pattern of peak ground acceleration (PGA), and thus likely the pattern of earthquake-triggered landsliding. To investigate this, we have modeled the propagation of seismic waves in a generic ridge-and-valley topography, using the impedance operator method (Haines et al., 2004a,b). The model topography corresponds to a set of mountain ridges oriented parallel to a seismogenic thrust fault, and set within its hanging wall, or to a set of ridges perpendicular to the fault and located immediately along-strike from the earthquake source. This comprises the majority of individual ridges in our study areas. The substrate is assumed to be uniform and non-layered, to reduce model complexity and isolate the topographic site effects. Layering of the geological substrate is known to be an important cause of site effects (Geli et al., 1988), and it can have a greater influence on PGA than topography, but we seek to explain a landslide pattern with a characteristic length scale greater than that of the geological grain of our study areas.

Although a 3D model is required to fully describe topographic site effects, 2D topographic profiles adequately capture the essential geometry of mountain ridges, and allow exploration of key features of the observed landslide patterns. Here, we present results for two profiles, defined to reflect the topographies of our study areas. Both profiles have ridge flank lengths equivalent to the average slope length of the Finisterre Mountains, l_m = 1.6 km. One has smooth, slightly concave-up slopes, defined by the average Finisterre Mountains ridge profile in which the convex-up knick points have been replaced by straight slopes with a gradient of 27°, that is the average gradient of locations immediately above the convex-up knick point (Fig. 6). This

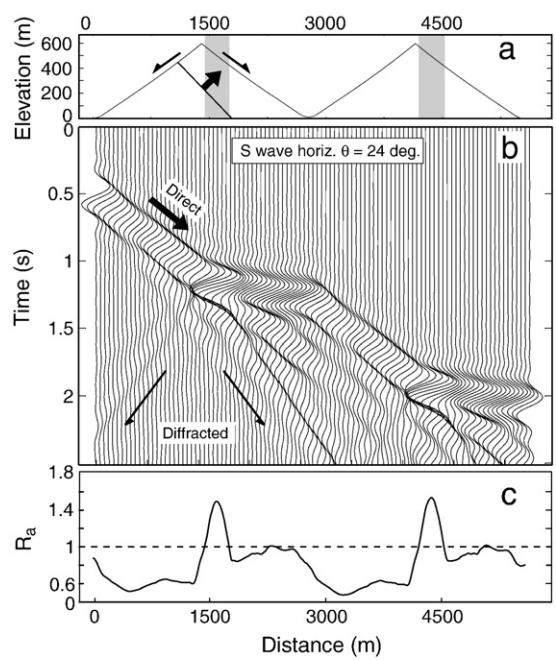

Fig. 6. a: Topographic profile consisting of two adjacent mountain ridges (precise geometry is detailed in the main text). b: Synthetic accelerogram (ground acceleration recorded along the surface with time) generated along the topographic profile. This accelerogram is for the horizontal component of an S wave delta pulse [0–6 Hz] arriving from the left at an angle of 24° with vertical. The associated PGA ratio R_a is shown in (c). The direct wave interferes constructively with the diffracted wave generated at the ridge crest, causing amplification of the PGA on the ridge flank facing away from the wave source.

profile approximates the geometry of ridges found in the Northridge area and central west Taiwan. The other is the average Finisterre Mountains ridge, including a convexity in the lower slope segment above an inner gorge. In order to capture the pattern of amplification of PGA across a ridge and valley, we have extended the model topographic profile to include two adjacent ridges. The model substrate has a density of 2700 kg m^{-3}, and quality factors $Q^{-1}=0.01$ and 0.02 for P and S waves, respectively. In our model runs we have used plain pressure wave (P) and shear wave (S) pulses (sinc functions of particle velocity) arriving from the left side of the topographic profile with a varying angle of incidence θ (measured with respect to the vertical). The velocity of P and S waves is set at 3400 m s^{-1} and 2800 m s^{-1}, respectively, which is only of arbitrary significance since the medium is homogeneous. In fact, for a model topography of a given size, other wave speeds would induce the same amplification pattern, but at different wave lengths.

For a triangular ridge with homogeneous substrate, and a base width W and height h, the maximum ridge crest amplification of the vertical component of a monofrequential P wave, is obtained for a wavelength $\lambda=4W$. Similarly, the maximum amplification of the horizontal component of the S wave is obtained for $\lambda=4h$ (Bouchon, 1996). Thus, the optimal wave frequencies are $f_p=V_p/4W$ and $f_s=V_s/4h$. For our model setting, the optimal frequencies are $f_p=0.25$ Hz and $f_s=1.3$ Hz. However, inner gorges and mid-slope knick points in the model topography have a shorter length scale and are likely to introduce amplification processes that are optimal at higher frequencies. Therefore we have used a pulse wave with a frequency content of [0–6 Hz], sampled at 0.02 Hz intervals.

Fig. 6 shows, as an example, the horizontal component of the accelerations of the free surface of the model topographic profile without inner gorges, generated by an S wave with angle of incidence $\theta=24°$. Constructive interference of the direct wave with refracted waves generated at the ridge crests amplifies acceleration on the ridge sides facing away from the wave source. The degree of amplification is given by the amplification ratio R_a, defined as the peak ground acceleration at a given point of the profile normalized by the amplitude in the absence of topography (Fig. 6c). At the point of maximum amplification, located in the upper quart of ridge slopes, $R_a=1.5$, implying a significant net increase of ground shaking. Near the central valley floor PGA is virtually unchanged, but elsewhere along the topographic profile, and especially on slopes facing the wave source, significant de-amplification of PGA has occurred.

The real amplification ratio of PGA for P and S waves is the summed effect of their horizontal and vertical components. For a given wave, $R^v{}_a$ and $R^h{}_a$ are the values of R_a for the vertical and horizontal component, respectively. Then, the modulus

$$\sqrt{(R_a^v)^2+(R_a^h)^2}>1 \tag{3}$$

defines the zones of net amplification of ground acceleration with respect to the energy carried by the incoming wave. Similarly, modulus values below 1 define zones of net damping. The value of the modulus is shown in Fig. 7. Significant amplification is observed for the S wave, near the ridge crest, where the modulus reaches a value of 1.5. The location of peak amplification shifts into the ridge slope facing away from the wave source as θ increases, but remains within the upper quart of the slope. Net damping of S waves occurs near the ridge base for low angles of incidence, and the zone of damping expands up slope into the ridge slope facing the wave source as θ increases. The pattern of amplification of the P wave is altogether less strong, but a minor net amplification of ground acceleration occurs at the ridge crest for all angles of wave incidence. In the following, we focus on the topographic site effects on S waves.

Fig. 8 shows the evolution of R_a with the angle of incidence θ, for the horizontal and vertical components of the S wave. Overall, R_a decreases with increasing θ for the horizontal component of the S wave (Fig. 8a), and increases with increasing θ for the vertical one (Fig. 8b). This is due to the rotation of the wave components with the angle of wave incidence. The highest amplification ratios are found near the ridge crests for both components, and the offset of the point of maximum amplification into the ridge side facing away from the wave source increases with the angle of wave incidence. Secondary amplification peaks occur near the central valley, but only for the vertical component. Importantly, it should be noted that $R_a<1$ for the vertical S wave component throughout the model domain, with a maximum amplification ratio $R_a=0.9$. The highest amplification ratios ($R_a>1.5$) are found for the horizontal component.

Landslide clustering is not necessarily related to net amplification of ground motion, but it is controlled by the variation of the amplification ratio R_a along the topographic profile for a given angle of wave

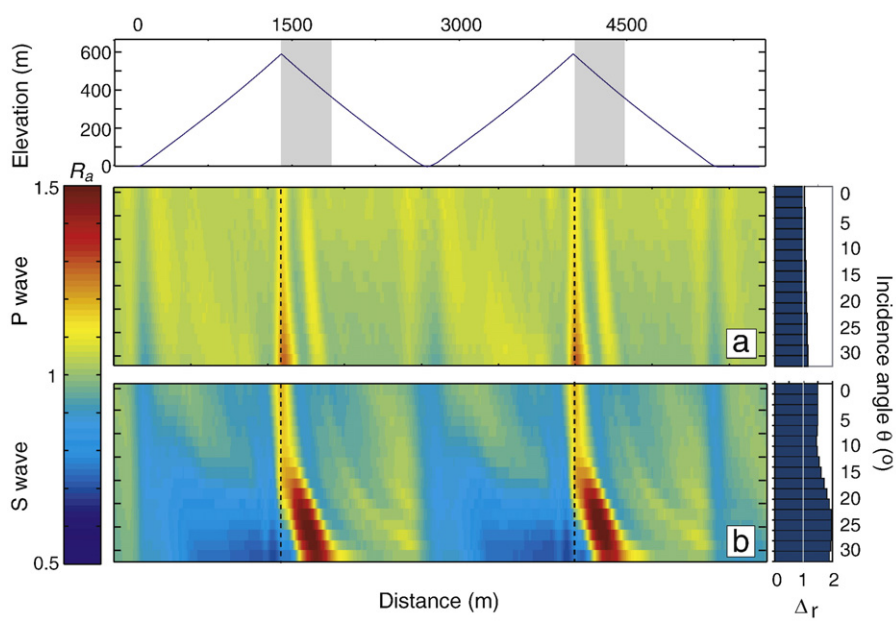

Fig. 7. Variation along the free topographic surface of two adjacent triangular ridges of the real amplification ratio (modulus) of PGA for P waves (a) and S waves (b) with angle of wave incidence. The net increase/damping of ground acceleration is defined with respect to the accelerations generated by impact of the same waves on a flat surface (set at 1).

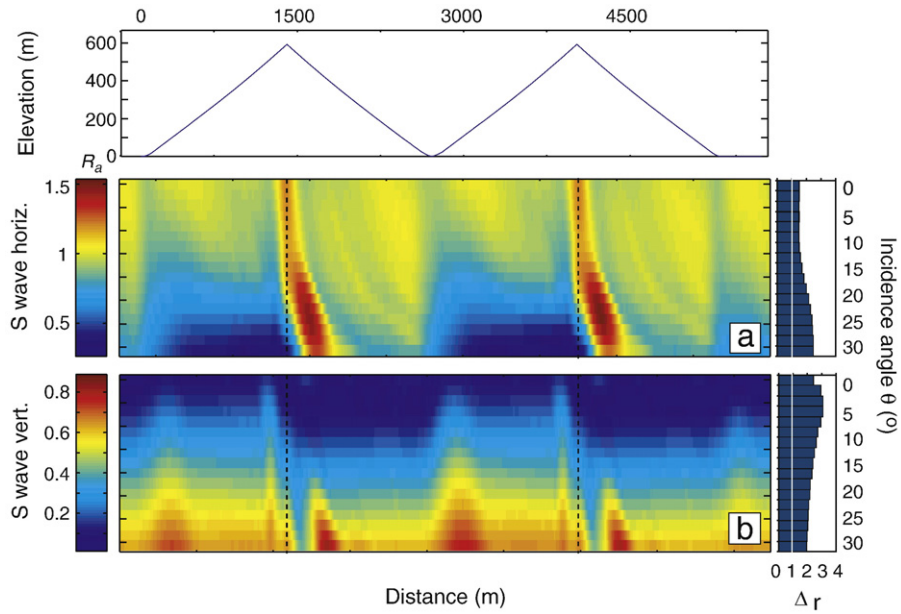

Fig. 8. Variation along the free topographic surface of two adjacent triangular ridges of the (de)-amplification ratio R_a of PGA on the horizontal (a) and the vertical (b) components of S plain wave pulses (0–6 Hz) with the angle of incidence. Δ_r (Eq. (3)), expresses the mean variation of the amplification ratio along the profile for a given angle of incidence, and equals 1 for a flat topography.

incidence θ. To determine the degree of variability, or focusing of PGA within the model topography, we have defined the variation ratio $\Delta_r(\theta)$ as

$$\Delta_r(\theta)=\frac{R_{a\ max}}{\frac{1}{n}\sum_{x_{min}}^{x_{max}} R_{an}(\theta)}, \tag{4}$$

where $R_{a\ max}$ and R_{an} are the maximum and the mean value of R_a observed along the profile for a given θ. Δ_r is equal to 1 in a flat topography. Values of Δ_r well above 1 indicate that the amplification ratio varies along the topographic profile, giving rise to distinct zonation of the PGA. It is clear that the P wave (Fig. 7a) does not contribute significantly to the focusing of PGA, and thus the clustering of landslides, because Δ_r is close to unity everywhere along the profile. In contrast, the model results reveal substantial focusing of PGA due to topographic site effects on S waves (Figs. 7b and 8). This effect is strongest near ridge crests ($\Delta_r > 1.5$), but it is also significant ($\Delta_r \geq 2$) at the base of ridge slopes facing the wave source for the vertical component of S waves with a high angle of incidence ($\theta > 15°$), even though no real amplification is observed there (Fig. 8b).

Taken together, these model results suggest that ridge-and-valley topography has little effect on incoming P waves, but a strong effect on S waves, giving rise to a significant amplification of peak ground accelerations at or near ridge crests. This is a likely cause of the clustering of landslides near ridge crests observed in all three

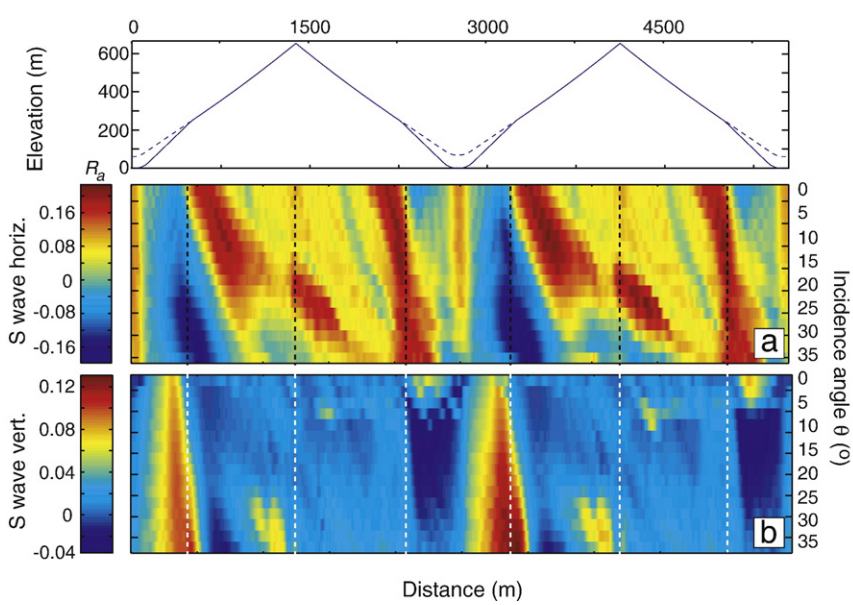

Fig. 9. Difference of R_a between a topographic profile with inner gorges (solid line) and without inner gorges (dashed line) for the horizontal (a) and vertical (b) components of an S wave pulse.

epicentral areas. High rates of landsliding near the base of ridges in central west Taiwan and the southern Finisterre Mountains could be due to focusing of strong ground motion associated with the vertical component of S waves with a high angle of incidence. In these areas, lower slopes may be inherently prone to failure due to the focusing of groundwater outflow, as discussed earlier, and the presence of mechanically weak colluvial deposits. However, in the Finisterre Mountains, the presence of inner gorges bounded by distinct, convex-up hillslope knick points may cause additional topographic site effects on seismic waves that should also be taken into consideration.

To explore this we have repeated our simulations with a topographic profile composed of two average Finisterre Mountains ridges bounding a central valley with an inner gorge (Fig. 9), and defined dR_a as the difference of R_a along in the Finisterre Mountains profile and R_a along the equivalent profile without gorges. dR_a is small for P waves, but significant for both components of S waves (Fig. 9). The horizontal component of S waves is amplified by the convex-up knick point. For low angles of wave incidence this effect is located on the knick point, but with increasing θ it shifts in the direction of movement of the incoming waves, towards the ridge crest in slopes facing the wave source, and towards the valley in slopes facing the other way. At high angles of incidence (θ>20°) the topographic site effects of the knick point on the horizontal component of S waves also include further amplification of peak ground accelerations at or near ridge crests. The inner gorge and knick points cause amplification of the vertical component of incoming S waves in gorge walls facing the wave source. Thus, the addition of local convexities to a simple triangular ridge can introduce important changes to the pattern of surface accelerations along the topographic profile. The presence of inner gorges bounded by convex-up knick points along many valleys in the Finisterre Mountains causes localized amplifications of incoming S waves over and above those associated with the triangular cross profile of the principal ridges. These additional amplifications primarily affect the lower ridge slope segments where clustering of earthquake-triggered landslides has been observed (Figs. 3 and 4).

5.3. Topography or topographic site effect?

We have shown that clustering of earthquake induced landslides occurs where topographic slopes are steepest and where seismic ground accelerations are greatest. Amplification of seismic waves is associated with convexities in mountain ridges, such as ridge crests and ridge flank knick points, and the steepest slopes are systematically found nearby. This makes it difficult to discern the primary control on the location of earthquake induced landslides from a global analysis of their clustering. However, the asymmetric amplification of oblique incoming seismic waves across a mountain ridge can be used to determine the roles of topography and topographic site effects in setting landslide patterns. In our simulations, zones of maximum ground acceleration are located near ridge crests for vertically incident waves. With increasing angle of wave incidence, the amplification maxima shift progressively into ridge flanks facing away from the wave source. Thus the pattern of ground accelerations is only symmetric in ridges directly above the earthquake hypocenter. Elsewhere, the pattern is asymmetric.

Slope orientation is not uniformly distributed in mountain ranges. Instead, a relatively large proportion of slopes face into the dipping plain of the range bounding fault. In the south flank of the Finisterre Mountains, for example, slopes dipping to the SW are twice as abundant as slopes dipping with the Ramu-Markham fault to the NE (Fig. 10). To correct for this effect, we have normalized the absolute frequency of landslides with a given orientation for the relative frequency of topographic slopes with that orientation. The normalized distributions of landslide orientations in our study areas are strongly asymmetric. In the Finisterre Mountains, most landslides occurred to the east of the earthquake epicenters. There, slopes facing to the SE and away from the seismic source were four times more likely to fail than slopes dipping toward the epicenter (Fig. 10a). In Taiwan, most of the landslides in our data set were located to the south of the earthquake epicenter, and in slopes facing to the SSW, away from the epicenter, failure rates were five times higher than in slopes dipping toward the epicenter (Fig. 10b). These strongly oriented landslide distributions indicate that topographic site effects dominate the location of earthquake induced landslides in central west Taiwan and the southern Finisterre Mountains, and that the rate of failure of the steepest slopes in mountain ranges is set by the local peak ground acceleration.

Landslides in the Northridge epicentral area have occurred preferentially on south-facing slopes in the Santa Susanna and San Miguel Mountains (Fig. 10c). Ridge crest clustering of landslides is strongest in this region, implying significant topographic site effects on seismic waves, but the earthquake hypocenter was located to the south of the Santa Susanna Mountains, and our model results anticipate location of landslides on north-facing slopes in this study area. Parise and Jibson (2000) invoke a geological control in the Northridge epicentral area. The dominant dip of geological strata in this region is to the south, and slope failure along bedding planes may have been important. However, the attitude of rock layers does not appear to be a first-order control on landslide aspect in the western Taiwan and the Finisterre Mountains. Most landslides triggered by the Northridge earthquake were shallow, displacing soil and regolith, and a dependence of soil production rate on slope aspect could be a major control on the landslide orientation in the epicentral area. In the arid landscapes of the southwest United States, physical breakdown of exposed bedrock is driven by diurnal heating and cooling due to solar irradiation (Mcfadden et al., 2005). This effect is strongest on south-facing slopes with maximal exposure to direct irradiation, and weakest on north-facing slopes. We have not found any published evidence of aspect-dependent soil production in the Northridge area, but anticipate that the location of earthquake induced landslides on south-facing slopes may reflect the relative abundance of soil and colluvium on those slopes.

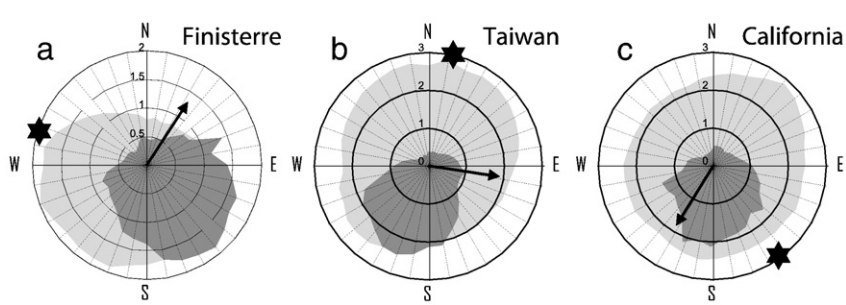

Fig. 10. Distribution of orientation of the slopes (in %, light grey) and normalized distribution of orientation of the landslides (dark grey) in a) the Finisterre Mountains, b) Taiwan and c) California. Arrows indicate the direction of the fault dip. Stars indicate the relative mean position of the epicenter.

6. Conclusion

The rate and location of earthquake induced landsliding are set by the intensity and pattern of peak ground shaking. On a regional scale, the rate of landsliding decreases systematically away from earthquake epicenters as seismic waves spread and attenuate (Meunier et al., 2007), and topographic site effects on seismic waves dominate the landslide pattern on the scale of an individual mountain ridge. Impedance operator modeling of seismic waves traveling in ridge-and-valley topography shows that diffraction and interference of seismic waves in topographic ridges causes amplification of ground accelerations near ridge crests. This effect is strongest in S waves, and the exact location of amplification maxima depends on the angle of wave incidence. Oblique incidence of seismic waves causes amplification maxima to shift away from ridge crests and into ridge flanks facing away from the earthquake epicenter. Secondary amplification maxima are predicted at smaller, convex-up knick points within ridge flanks. These model results largely match patterns of landsliding caused by recent, large earthquakes in California, Taiwan and Papua New Guinea. In all epicentral areas, landslides cluster around ridge crests, where peak ground accelerations are likely to have been greatest. They preferentially affect the steepest topographic slopes. Secondary landslide clusters have been found near prominent knick points above inner gorges along the main valleys of the Finisterre Mountains. There, and in the epicentral area of the Chi-Chi earthquake, Taiwan, landslide rates were highest in slopes facing away from the earthquake epicenter. However, in the epicentral area of the Northridge earthquake landslide orientation is not according to topographic site effects on oblique incoming seismic waves, and may instead reflect the dependence of weathering and soil production on slope aspect. Nevertheless, the strength and detail of the match of observations and model results suggest that peak ground acceleration is a principal control on the location of earthquake induced landslides in mountain regions, and so knowledge of topographic site effects and the attenuation of seismic waves is an important tool in the prediction of spatial patterns of landslide intensity.

Clustering of landslides due to topographic site effects on seismic waves has important consequences for the topographic evolution of areas where earthquake-triggered mass wasting dominates the long-term erosion. Landslides remove the steepest slope segments, reducing the average slope of the landscape. If this effect is strongest near ridge crests due to amplification of surface accelerations, then ridge crests are progressively rounded as a result. Rounding of ridges on a 102 m scale is found in all four mountain ranges considered in this study. It may be a fingerprint of the persistent location of earthquake induced landslides.

Acknowledgments

This work was supported by European Commission FP6 STREP FORESIGHT and the Leverhulme Trust. NH thanks the Geological Survey of Papua New Guinea for generous logistical support of field work in the Finisterre Mountains. Hongey Chen has facilitated access to landslide data for Taiwan, and Colin Stark first developed the landslide location analysis shown in Fig. 3. We are grateful for two generous and constructive, yet anonymous reviews.

References

Abbott, L.D., Silver, E.A., Thompson, P.R., Filiwicz, M., Schneider, C., Abdorrias, 1994. Stratigraphic constraints on the development and timing of arc–continent collision in northern Papua New Guinea. J. Sediment. Res. 124, 169–183.

Abbott, L.D., Silver, E.A., Anderson, R.S., Smith, R., Ingle, J.C., Kling, S.A., Haig, D., Small, E., Galewsky, J., Sliter, W., 1997. Measurement of tectonic surface uplift in a young collisional mountain belt. Nature 385, 501–507.

Batt, G.E., 1997. The crustal dynamics and tectonic evolution of the Southern Alps, New Zealand: Insights from new geochronological data and fully-coupled thermo-dynamical finite element modeling. Ph.D. thesis, Aust. Natl. Unv., Canberra, A.C.T.

Benites, R.A., Haines, A.J., 1994. Quantification of seismic wavefield amplification by topographic features. Research Report to the Earthquake Commission, New Zealand. 108 pp.

Bouchon, M., 1973. Effect of topography on surface motion. Bull. Seismol. Soc. Am. 63, 615–632.

Bouchon, M., Baker, J., 1996. Seismic response of a hill: the example of Tarzana, California. Bull. Seismol. Soc. Am. 86, 66–72.

Bouchon, M., Schultz, C.A., Toksoz, M.N., 1996. Effect of three dimensional topography on seismic motion. J. Geophys. Res. 101, 835–846.

Brune, J.N., 2001. Shattered rock and precarious rock evidence for strong asymmetry in ground motions during thrust faulting. Bull. Seismol. Soc. Am. 91, 441–447.

Bull, W.B., Cooper, A.F., 1986. Uplifted marine terraces along the Alpine fault, New Zealand. Science 234, 1225–1228.

Burbank, D.W., Leland, J., Fielding, E., Anderson, R.S., Brozovic, N., Reid, M.R., Duncan, C., 1996. Bedrock incision, rock uplift and threshold hillslopes in the northwestern Himalayas. Nature 379, 505–510.

Carson, M.A., Kirkby, M.J., 1972. Hillslope—Form and Process. Cambridge Geogr. Stud., vol. 3. Cambridge Univ. Press, New York.

Chen, W.S., Chen, Y.G., Chang, H.C., Lee, Y.H., Lee, J.C., 2001. Palaeoseismic study of the Chelungpu fault in the Wanfung area. West. Pac. Earth Sci. 1, 499–506.

Dadson, S.J., Hovius, N., Chen, H., Dade, W.B., Hsieh, M.L., Willett, S.D., Hu, J.C., Horng, M.J., Chen, M.C., Stark, C.P., Lague, D., Lin, J.C., 2003. Links between erosion, runoff variability and seismicity in the Taiwan orogen. Nature 426, 648–651.

Dadson, S.J., Hovius, N., Chen, H., Dade, W.B., Lin, J.C., Hsu, M.L., Lin, C.W., Horng, M.J., Chen, T.C., Milliman, J., Stark, C.P., 2004. Earthquake-triggered increase in sediment delivery from an active mountain belt. Geology 32, 733–736.

Davies, H.L., Lock, J., Tiffin, J.L., Okuda, Y., Murakami, F., Kisimoto, K., 1987. Convergent tectonics in the Huon Peninsula region, Papua New Guinea. Geo-Mar. Lett. 7, 143–152.

Davis, L.L., West, L.R., 1973. Observed effects of topography on ground motion. Bull. Seismol. Soc. Am. 63, 283–298.

Densmore, A.L., Hovius, N., 2000. Topographic fingerprints of bedrock landslides. Geology 28, 371–374.

Geli, L., Bard, P.-Y., Jullien, B., 1988. The effect of topography on earthquake ground motion: a review and new results. Bull. Seismol. Soc. Am. 78, 42–63.

Griffiths, G.A., McSaveney, M.J., 1983. Distribution of mean annual precipitations across some steepland regions of New Zealand. N.Z. J. Sci. 26, 197–209.

Haines, A.J., Hulme, T., Yu, J., 2004a. General elastic wave scattering problems using an impedance operator approach I. Mathematical development. Geophys. J. Int. 159, 643–657.

Haines, A.J., Hulme, T., Yu, J., 2004b. General elastic wave scattering problems using an impedance operator approach II. Two dimensional isotropic validation and examples. Geophys. J. Int. 159, 658–666.

Harp, E.L., Jibson, R.W., 1995. Inventory of landslides triggered by the 1994 Northridge, California earthquake. US Geological Survey Open-File Report 95-213. 17 pp.

Harp, E.L., Jibson, R.W., 1996. Landslides triggered by the 1994 Northridge, California earthquake. Bull. Seismol. Soc. Am. 86, 319–332.

Hauksson, E., Jones, L.M., Hutton, K., 1995. The 1994 Northridge earthquake sequence in California: seismological and tectonic aspects. J. Geophys. Res. 100, 12335–12355.

Hovius, N., Stark, C.P., Allen, P.A., 1997. Sediment flux from a mountain belt derived by landslide mapping. Geology 25, 231–234.

Hovius, N., Stark, C.P., Tutton, M.A., Abbott, L.D., 1998. Landslide-driven drainage network evolution in a pre-steady-state mountain belt: Finisterre Mountains, Papua New Guinea. Geology 26, 1071–1074.

Hovius, N., Stark, C.P., Chu, H.T., Lin, J.C., 2000. Supply and removal of sediment in a landslide dominated mountain belt: Central Range, Taiwan. J. Geol. 108, 73–89.

Iverson, R.M., 2000. Landslide triggering by rain infiltration. Water Resour. Res. 36, 1897–1910.

Iverson, R.M., Reid, M.E., 1992. Gravity-driven groundwater flow and slope failure potential, 1, elastic effective-stress model. Water Resour. Res. 28, 925–938.

Johns, R.J., 1986. The instability of the tropical ecosystem in New Guinea. Blumea 31, 341–371.

Kayen, R.E., Mitchell, J.K., Seed, R.B., Nishio, S., 1998. Soil liquefaction in the east bay during the earthquake. The Loma Prieta, California, Earthquake of October 17, 1989—Liquefaction. U.S. Geological Survey Professional Paper, vol. 1551-B, pp. 61–86.

Keefer, D.K., 1984. Landslides caused by earthquakes. Bull. Geol. Soc. Am. 95, 406–421.

Keefer, D.K., 1994. The importance of earthquake-induced landslides to longterm slope erosion and slope-failure hazards in seismically active regions. Geology 10, 265–284.

Keefer, D.K., 2000. Statistical analysis of an earthquake-induced landslide distribution—the 1989 Loma Prieta, California event. Eng. Geol. 58, 213–249.

Keefer, D.K., 2002. Investigating landslides caused by earthquakes—a historical review. Surv. Geophys. 23, 473–510.

Kelsey, H.M., 1988. Formation of inner gorges. Catena 15, 433–458.

Korup, O., 2006. Effects of deep-seated bedrock landslides on hillslope morphology, Southern Alps, New Zealand. J. Geophys. Res. 111, F01018. doi:10.1029/2004JF000242.

Lavé, J., Burbank, D., 2004. Erosion rates and patterns in the Transverse Ranges (California). J. Geophys. Res. 109. doi:10.1029/2003JF000023.

Lee, W.H.K., Shin, T.C., Kuo, K.W., Chen, K.C., Wu, C.F., 2001. CWB free-field strong motion data from the 921 Chi-Chi earthquake. Bull. Seismol. Soc. Am. 91, 1370–1376.

Lin, M.L., Wang, K.L., Chen, T.C., 2000. Characteristics of the slope failure caused by Chi-Chi earthquake. In: Loh, C.H., Liao, W.I. (Eds.), International Workshop on Annual Commemoration of Chi-Chi Earthquake (III). National Center for Research on Earthquake Engineering, Taipei, pp. 199–209.

Lin, G.W., Chen, H., Hovius, N., Horng, M.J., Dadson, S., Meunier, P., Lines, M., in press. Effects of the 1999 chi-chi earthquake on patterns and rates of mass wasting and fluvial sediment transfer in the Chenyoulan river catchment, Taiwan. *Earth Surf. Process. Landf.*

Mcfadden, L.D., Eppes, M.C., Gillespie, A.R., Hallet, B., 2005. Physical weathering in arid landscapes due to diurnal variation in the direction of solar heating. Bull. Geol. Soc. Am. 117, 161–173.

Meunier, P., Hovius, N., Haines, A.J., 2007. Regional patterns of earthquake-triggered landslides and their relation to ground motion. Geophys. Res. Lett. 34, L20408. doi:10.1029/2007GL031337.

Montgomery, D.R., 1993. Compressional uplift in the central California Coast Ranges. Geology 21, 543–546.

Montgomery, D.R., 2001. Slope distributions, threshold hillslopes, and steadystate topography. Am. J. Sci. 301, 432–454.

Oldham, R.D., 1899. Report of the great earthquake of 12th June 1897, Mem. Geol. Surv. India, 379 p. (Reprinted by Geol. Surv. of India, Calcutta, 1981.)

Parise, M., Jibson, R.W., 2000. A seismic landslide susceptibility rating of geologic units based on analysis of characteristics of landslides triggered by the 17 January, 1994 Northridge, California earthquake. Eng. Geol. 58, 251–270.

Pezzopane, S.K., Wesnousky, S.G., 1989. Large earthquakes and crustal deformation near Taiwan. J. Geophys. Res. 94, 7250–7264.

Ramsey, L.A., Hovius, N., Lague, D., Liu, C.-S., 2006. Topographic characteristics of the submarine Taiwan orogen. J. Geophys. Res. 111, F02009. doi:10.1029/2005JF000314.

Ripper, I.D., Letz, H., 1991. Distribution and Origin of Large Earthquakes in the Papua New Guinea Region, 1900–1989. Geological Survey of Papua New Guinea, Port Moresby. Geological Survey of Papua New Guinea Report 91/5, 74 pp.

Shakal, A., Huang, M., Darragh, R., Cao, T., Sherburne, R., Malhotra, P., Cramer, C., Sydnor, R., Graizer, V., Maldonado, G., Peterson, C., Wampole, J., 1994. CSMIP Strong Motion Records from the Northridge, California, Earthquake of 17 January 1994, Report OSMS 94-07. Calif. Div. Mines Geol., Sacramento, California.

Shin, T.C., Teng, T.L., 2001. An overview of the 1999 Chi-Chi, Taiwan, earthquake. Bull. Seismol. Soc. Am. 91, 895–913.

Spudich, P., Hellweg, M., Lee, W.H.K., 1996. Directional topographic site response at Tarzana observed in aftershocks of the 1994 Northridge, California, earthquake: implications for mainshock motions. Bull. Seismol. Soc. Am. 86, 193–208.

Stevens, C., McCaffrey, R., Silver, E.A., Sombo, Z., English, P., van der Kevie, J., 1998. Mid-crustal detachment and ramp faulting in the Markham Valley, Papua New Guinea. Geology 26, 847–850.

Swiss Reinsurance Company 2000. Natural catastrophes and man-made disasters in 1999, Economic Research and Consulting. Zurich, Sigma No. 2/2000, 35 p.

Tippett, J.M., Kamp, P.J.J., 1993. Fission track analysis of the late Cenozoic vertical kinematics of continental Pacific crust, South Island. N.Z. J. Geophys. Res. 98, 16119–16148.

Tutton, M.A., Browne, T.J., 1994. A review of damage caused by the 1993 Finisterre Range earthquake, Papua New Guinea. In: Rogerson, R. (Ed.), Proceedings of the PNG Geology, Exploration and Mining Conference 1994, Lae, pp. 33–41.

Walcott, R.I., 1984. The kinematics of the plate boundary zone through New Zealand: a comparison of short- and longterm deformations. Geophys. J. R. Astron. Soc. 52, 137–164.

Wang, C.-Y., Wang, C.-H., Manga, M., 2004. Coseismic release of water from mountains: evidence from the 1999 (M_w=7.5) Chi-Chi, Taiwan, earthquake. Geology 32, 769–772.

Wells, A., Yetton, M.D., Duncan, R.P., Stewart, G.H., 1999. Prehistoric dates of the most recent Alpine Fault earthquakes, New Zealand. Geology 27, 995–998.

Wu, C.C., Kuo, Y.H., 1999. Typhoons affecting Taiwan: current understanding and future challenges. Bull. Am. Meteorol. Soc. 80, 67–80.

Youd, T.L., Perkins, D.M., 1978. Mapping liquefaction-induced ground failure potential. J. Geotech. Eng. Div., ASCE 104, 433–446.